ADVANCED
FUNCTIONAL
MATERIALS

FULL PAPER

Plastic Dissipation Mechanisms in Periodic Microframe-Structured Polymers

By *Lifeng Wang, Mary C. Boyce,* * *Cheng-Yen Wen,* and *Edwin L. Thomas*

Novel lightweight micro- and nanostructured materials are being used as constituents in hierarchically structured composites for providing high stiffness, high strength, and energy absorbing capability at low weight. Three dimensional SU-8 periodic microframe materials with submicrometer elements exhibit unusual large plastic deformations. Here, the plastic dissipation and mechanical response of polymeric microframe structures is investigated using micromechanical modeling of large deformations. Finite element analysis shows that multiple deformation domains initiate, stabilize, and then spread plasticity through the structure; simulated deformation mechanisms and deformation progression are found to be in excellent agreement with experimental observation. Furthermore, the geometry can be used to tailor aspects of 3D behavior such as effective lateral contraction ratios (elastic and plastic) during tensile loading as well as negative normal stress during simple shear deformation. The effects of structural geometry on mechanical response are also studied to tailor and optimize mechanical performance at a given density. These quantitative investigations enable simulation-based design of optimal lightweight material microstructures for dissipating energy.

1. Introduction

New design concepts for energy absorption materials, especially for personal protection applications, have attracted great interest in material science.[1] Novel lightweight micro- and nanostructured materials are being used as constituents in hierarchically structured composites for providing high stiffness, high strength, and energy absorbing capabilities.[2,3] Multifunctional microframe structures appear widely in nature, examples include cork,[4] the *Euplectella* sp. skeleton,[5] and sea urchin exoskeleton,[6] and possess optimized mechanical properties, which

inspire many man-made structural materials at micro- and macrolength scales. At the submicron scale, the constituent material of such porous cellular structures can present improved mechanical properties compared to that of the corresponding bulk materials.

Polymer microstructures with reduced feature size are anticipated to possess enhanced energy absorption capability over their bulk counterparts due to the size-scale dependence of the mechanical failure mode. For example, bulk scale brittle polymeric materials can exhibit highly ductile plastic deformations at small length scales;[7,8] below a critical film thickness, the failure strain of glassy polymers and thermosetting polymers can greatly increase.[9,10] Recently two-dimensional (2D) and three-dimensional (3D) SU-8 periodic microframe structural materials with submicrometer elements, low density, and feature sizes at the lengthscale of several hundreds of nanometers were fabricated using laser interference lithography.[11,12] These structures exhibit unusual large plastic deformations when subjected to complex multiaxial loading conditions with local failure strains reaching up to ∼300% in the thin members of 3D SU-8 microframes;[12] in particular, the images of deformed structural elements clearly depict the classic features of cold drawing of glassy polymer bars including neck initiation, neck stabilization, and neck propagation. Although the mechanical behavior of the microframe-structured materials has not yet been quantified, the unique characteristics of plastic deformation in the thin elements, including necking and subsequent mechanical stabilization and drawing into long fibrils, indicate the potential of these structures to function as highly dissipative elements in lightweight energy absorption materials.
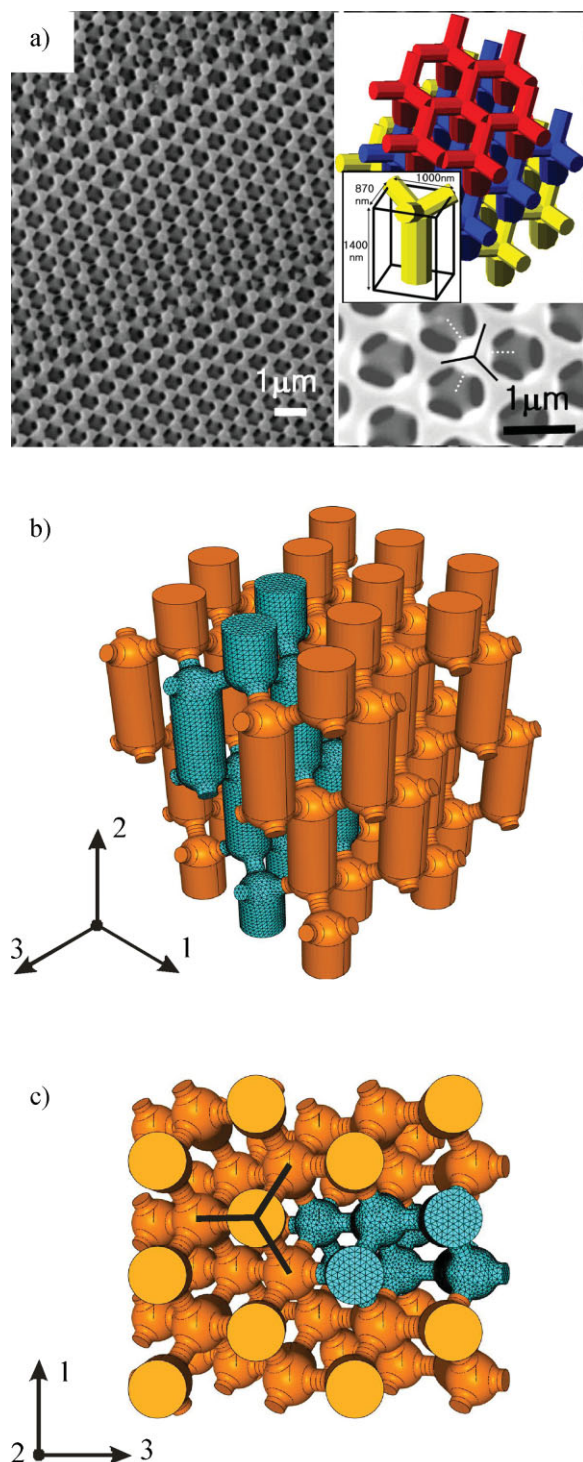
Here we investigate the plastic dissipation of 3D periodic SU-8 polymer microframe structures using micromechanical modeling (MM) to simulate the large deformations in tension, compression, and shear observed in these materials. MM is an efficient method to determine overall mechanical behavior of structural and composite materials based on the constituent material stress–strain behavior together with a periodic representative volume element (RVE) of the microstructure. MM also simultaneously captures details of the underlying deformation mechanisms governing the response.

[*] Prof. M. C. Boyce, Dr. L. F. Wang
Department of Mechanical Engineering
Massachusetts Institute of Technology
Cambridge, MA 02139 (USA)
E-mail: mcboyce@mit.edu
Dr. C. Y. Wen, Prof. E. L. Thomas
Institute for Soldier Nanotechnologies
Department of Materials Science and Engineering
Massachusetts Institute of Technology, Cambridge, MA 02139 (USA)

WILEY InterScience®
DISCOVER SOMETHING GREAT

Figure 1. 3D SU-8 microframe structure fabricated using interference lithography [12]. a) Scanning electron microscopy images of the 3D SU-8 microframe structure [12]. The small inset shows a perspective view of the structure with the basic motif of the four-functional element. b,c) Finite element-based micromechanical model of microframe structure from different viewpoints; the meshed RVE consists of six motifs (shown green).

2. Results and Discussion

2.1. Computational Approach

The RVE geometry is created based on the fundamental repeat unit of the microframe structure. Figure 1a depicts micrographs and schematics of the 3D structure under consideration; the inset schematic shows the basic motif comprised of a thicker vertical post and three thinner diagonal struts and its spatial arrangement. In order to implement boundary conditions on the RVE expediently, the 3D structure motif of the microframe structure consists of one thick post and six thinner obliquely oriented struts, each of one-half the length of a full strut. In each layer there are two motifs which capture not only the macroscopic deformation but also the local deformational characteristics. The RVE consists of six motifs arranged in the unit cell. Figure 1b and c shows the finite element-based micromechanical model of the structure with the six motifs of the RVE shown in green (with mesh), surrounded by five neighboring RVEs (orange) for illustration purposes. For this structure, the initial volume

Table 1. The processing routes of the SU-8 used in Refs. [8,11,12]

SU-8	Processing history	T_g (°C)
Beams	Soft bake 65 °C, 1 min and 95 °C, 3 min	155 (DMA)
	Exposed: 365 nm UV light, 270 mJ cm^{-2}	
Wen et al. [8]	Post-exposure bake: 65 °C, 1 min and 95 °C, 1 min	
	Developed in PGMEA and rinsed in IPA and dried	
Beams	Same procedure as above but with an additional	277 (DMA)
Wen et al. [8]	Hard bake: 180 °C, 5 min	
3D microframes	Soft bake: 95 °C, 10 min	100 (DSC)
	Exposed: 532 nm Nd:YAG laser, 5–10 J cm^{-2}	
Jang et al.[12]	Post-exposure bake: 65 °C, 5 min	
2D microframes	Same procedure as Ref. [12]	100 (DSC)
Choi et al.[11]		
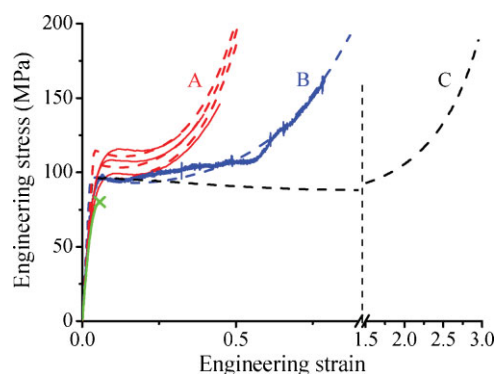
Figure 2. Engineering stress–strain behavior of SU-8 beams under uniaxial tension: experiments (solid lines) and constitutive model prediction (dashed lines). The A, B, and C curves present material properties of the material states characterized by draw ratios of 1.45, 1.75, and 3.0, respectively. Tensile tests conducted at the strain rates of 10^{-3}, 10^{-2}, and 10^{-1} s^{-1} are included for the SU-8A sample; the SU-8B and SU-8C behaviors are shown for a strain rate of 10^{-3} s^{-1}. Green line presents the brittle behavior of an SU-8 film.

Table 2. Material property constants for SU-8 with different material states (these model parameters have the same meanings with those in Refs. [15–17]).

| Elastic			Viscoplastic				Strain hardening			
Draw ratio	E [GPa]	ν	$\dot{\gamma}_0$ [10^5 s^{-1}]	ΔG [10^{-19} J]	s_0 [MPa]	s_{ss} [MPa]	h [MPa]	C_R [MPa]	N
1.45	3.3	0.33	4.62	1.78	103	98	300	12.0	1.42
1.75	3.3	0.33	4.62	1.78	103	98	300	12.0	1.90
3.0	3.3	0.33	4.62	1.78	103	98	300	12.0	8.00

fraction of polymer is 26%, which is consistent with experiments (∼30%).

The infinite periodic nature of the structure is captured through periodic boundary conditions.[13,14] The RVE can be subjected to any arbitrary macroscopic deformation gradient. In this study, the periodic RVEs are subjected to several loading conditions, including uniaxial tension in different directions, uniaxial compression, as well as simple shear. The average macroscopic response for each case is calculated through virtual work considerations.[13,14]

2.2. Material Properties

The stress–strain behavior of the SU-8 material inherent to the particular microframe material modeled in this study has not been measured. However, micrographs of the microframe structure after deformation clearly depict that the structural elements undergo extensive plastic deformation with elements exhibiting neck initiation, stabilization and propagation—i.e., the classic cold (below glass transition temperature) drawing process of a polymer. Hence, the SU-8 of interest exhibits elastic–plastic behavior with a clear yield stress, a regime of low strain hardening, followed by significant strain hardening at a stretch of around 3.0. Given that the stress–strain behavior for the microframe SU-8 material state was not available, the experimentally obtained stress–strain behavior of SU-8 processed into uniform cross-section beams via a different processing history[8] is used as to provide a representative SU-8 elastic–plastic behavior; the Wen et al. data is further supplemented here with additional tests to quantify the rate dependence of SU-8 (strain rates of 10^{-3}, 10^{-2}, and 10^{-1} s^{-1}). The different processing routes of the SU-8 materials are given in Table 1. Note that the first processing route of Table 1 produces a brittle material. Figure 2 depicts the experimental stress–strain behavior of uniform cross-section beams of SU-8 produced using the second processing route of Table 1; these samples exhibit the characteristic features of the tensile behavior of ductile polymers: initial linear elasticity, fol-

lowed by a rate-dependent yield stress, strain softening, and subsequent strain hardening at larger strains. As evident in Figure 2, the Wen et al. SU-8 materials exhibited a draw ratio that depended on the cross-section of the fabricated beam (higher draw ratio for smaller cross-section beam: draw ratio of 1.45 for a $25 \times 25\,\mu m^2$ and 1.75 for $1.6 \times 1.6\,\mu m^2$). The yield stress does not depend on specimen size. Furthermore, the stress–strain behavior of the SU-8 material of the microframe structure clearly differs from that of the Wen et al. SU-8 as evidenced by the experimentally observed draw ratio of ∼3.0 for the structural
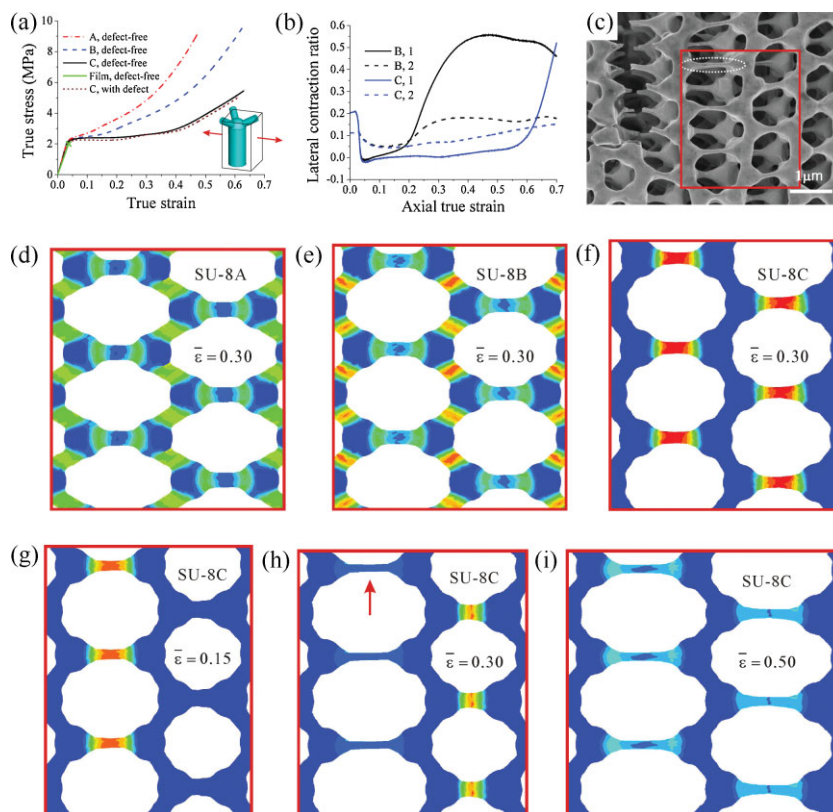
Figure 3. Mechanical response of microframe structures under macroscopic uniaxial tension in the 3-direction. a) Macroscopic true stress–strain curves of defect-free and imperfect microframe structure with various material properties. b) Lateral contraction ratios versus axial true strain using material property SU-8B and SU-8C. c) Experimental evidence of plastic deformation of structural elements with up to 300% plastic strain (e.g., circled beam) [12]. d–f) Simulated micrograph of defect-free microframe structure at a strain of 0.30 using material property SU-8A, SU-8B, and SU-8C, respectively. g–i) Simulated micrographs of microframe structure with imperfections at strains of 0.15, 0.30, and 0.5, where beam (pointed out) strain is about 280%. The progression in strain is in agreement with the experimental observations as depicted in the SEM image (Fig. 3c).

Adv. Funct. Mater. **2009**, *19*, 1343–1350

© 2009 WILEY-VCH Verlag GmbH & Co. KGaA, Weinheim

WILEY
InterScience®
DISCOVER SOMETHING GREAT

1345

elements of the microframe compared to the 1.45 and 1.75 draw ratios of the Wen et al. materials; data on the yield stress is not available for comparison. Since the processing of the SU-8 beams[8] is not identical to the SU-8 in the microframes,[12] the stress–strain measurements only serve as an approximation for the SU-8 elastic–plastic stress–strain behavior to capture the plasticity experimentally observed in the deformed microframes;[12] material draw ratios will be varied in the simulations to examine this effect on the microframe deformation mechanics.

A constitutive model[15–17] for the large strain, rate dependent elastic–viscoplastic behavior of glassy polymers is used to capture the features of the observed stress–strain behavior for SU-8 material states. From the stress–strain curves of Figure 2, we have determined three sets of material constants for SU-8 beams which correspond to material states with draw ratios of 1.45, 1.75, and 3.0. To capture these behaviors, all properties were taken to be the same except the strain hardening properties were changed to provide the proper draw ratio for each case, including a draw ratio of 3.0 for the microframe case. Properties are listed in Table 2. Note that here the parameter N is chosen to capture the limiting chain extensibility which in turn captures the draw ratio. Initial linear elasticity, rate-dependent yield, strain softening, and hardening behaviors are all captured by the model compared to experimental data. We use "SU-8A, SU-8B, and SU-8C" to denote the material properties for material states with draw ratios of 1.45, 1.75, and 3.0, respectively. For comparison, SU-8 film properties are also plotted in Figure 1b (the green curve), which exhibits a brittle failure at a strain of about 5%.[8] This is consistent with bulk behavior of fully cured SU-8.[18]

2.3. Micromechanical Simulation Results and Discussions

The simulated macroscopic uniaxial tension behaviors for the microframe structured materials are shown in Figure 3 for constituent materials SU-8A, SU-8B, and SU-8C for tension in the 3-direction. Figure 3a shows the overall microframe uniaxial stress–strain behaviors for each of the materials, demonstrating the influence of constituent material behavior on the microframe behavior. The microframe structure strain hardens at lower strains for the lower draw ratio materials. The influence of the constituent material strain hardening behavior also controls the progression of deformation within the microframe as evident in the snapshot contours of plastic strain rate (regions of active plastic deformation) taken at a macroscopic strain of $\bar{\varepsilon} = 0.30$ for SU-8A, SU-8B, and SU-8C in Figure 3d–f, respectively. In the case of SU-8A, the frame member axially aligned with the loading direction has plastically deformed and strain hardened such that, by $\bar{\varepsilon} = 0.30$, the active straining has progressed into the connecting nodes and further progressed into the diagonal members, resulting in macroscopic strain hardening occurring soon after yield for this material (Fig. 3a). In contrast,

for the material states characterized with a higher draw ratio, deformation is observed to be localized within the structural member aligned with the loading direction with necking down to a smaller diameter prior to neck stabilization and propagation
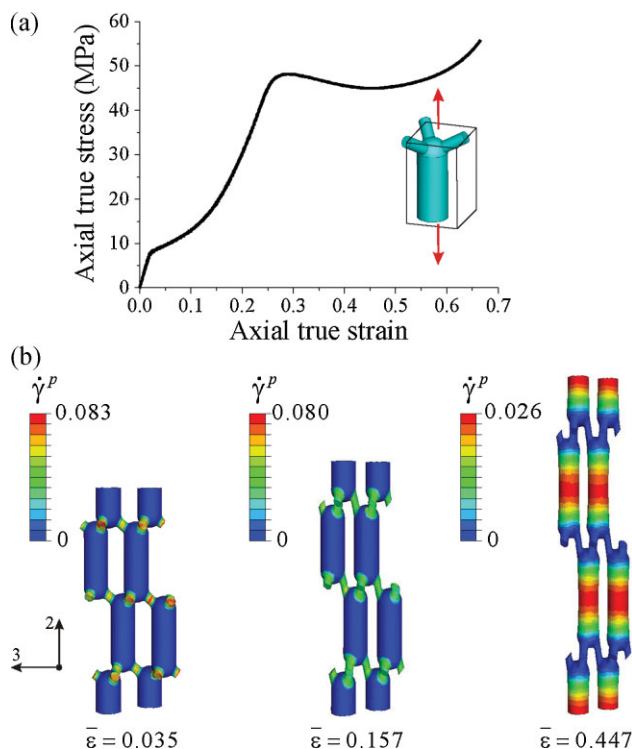
Figure 4. Mechanical response of the microframe structure under macroscopic uniaxial tension in the 2-direction. a) Simulated macroscopic stress–strain curves. b) Simulated results showing contours of plastic strain rate at increasing macroscopic tensile strain levels.
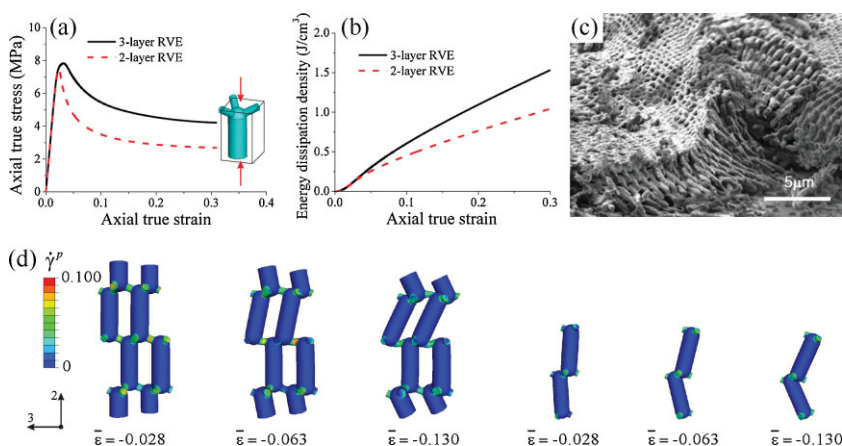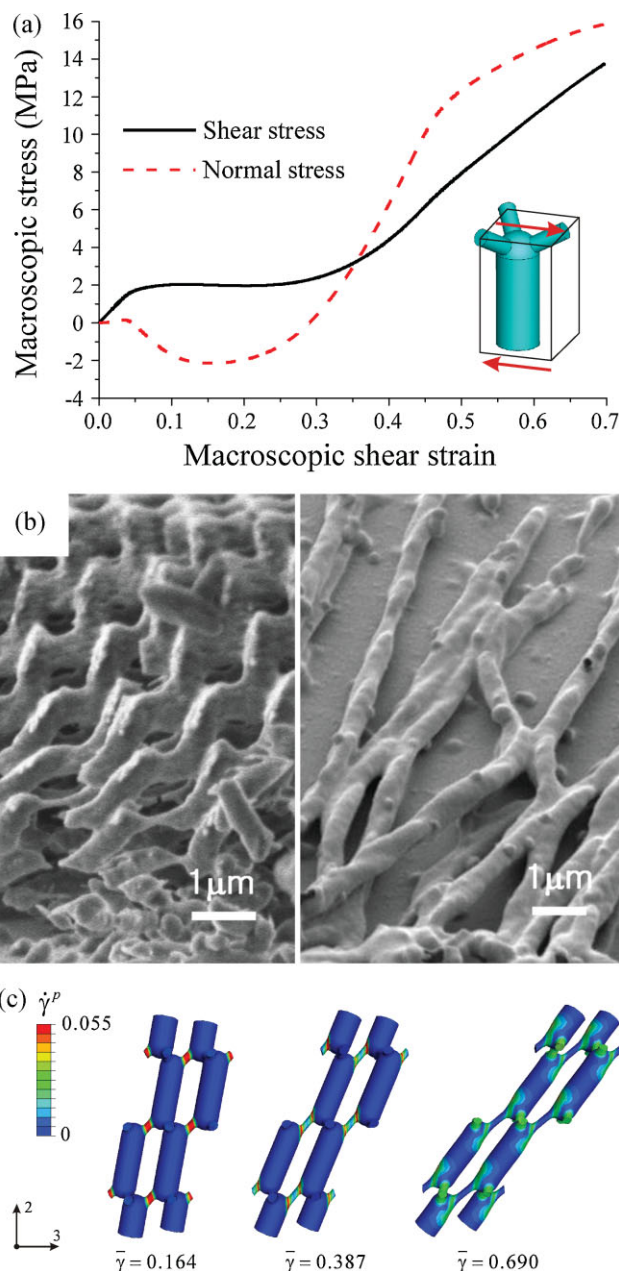

Figure 5. Mechanical response of the microframe structure under macroscopic uniaxial compression in the 2-direction. a) Simulated macroscopic stress–strain curves. b) Predictions of energy dissipation density as a function of compression strain. c) Micrograph of a portion of the film that was compressed, showing the collapsed microframe region at left [12]. d) Simulated contours of plastic strain rate for three- and two-layer RVEs at increasing macroscopic compression strains.

(Fig. 3e and f for SU-8B and SU-8C), corresponding to the delayed strain hardening behavior of the microframe structures shown in Figure 3a. (As an aside, using the macroscopic material properties in the microframe structure results in brittle failure of the microframe at a strain of 0.04 because the material locally reaches its failure strain.) Figure 3b shows the lateral contraction ratios as a function of axial true strain for the microframe structure with constituent materials SU-8B and SU-8C. The initial elastic Poisson ratios in the two directions are 0.11 and 0.20. When the struts parallel to the loading direction yield, the lateral contraction ratios become very small (approaching 0) since the macroscopic strain is accommodated by extension (with local necking and neck propagation) of the members coaxial with the applied load. Once the diagonal frame members begin to plastically deform, they rotate toward the axial direction, and the lateral contraction ratios increase; the macroscopic strain where this change in contraction behavior begins is found to depend on the draw ratio of the constituent material as seen in Figure 3b. This highly nonlinear contraction behavior under large strain (up to 1.5) has also been observed in some polymer cellular foams with an initially negative elastic Poisson's ratio.[19]

For perfect periodic microframe structures, struts located in the same periodic positions will experience the same deformation histories during a loading process (see Fig. 3d–f). However, in the experimental investigations, as shown in Figure 3c, struts in the same periodic positions experience different levels of deformation as a result of small irregularities/imperfections in the local structure geometry or material properties. To capture this effect, imperfections are introduced into the RVE in the form of slightly thinned struts at different locations. Deformation is then found to first localize in a thinned strut with neck initiation, stabilization, and propagation localizing in one layer of struts (Fig. 3g) and then, upon strain hardening of that layer, deformation progresses to the next layer of struts (Fig. 3h and i). This deformation progression capitalizes on the strain hardening behavior of a polymer which enables the spreading of deformation during plasticity rather than the localization of deformation in one layer until reaching failure. The predicted deformation progression mechanism agrees well with the experimental observation (see SEM image Fig. 3c). This spreading mechanism can be used to further enhance the design of energy dissipative microstructures.

Figure 4 shows the mechanical response of the microframe structure under macroscopic tension in the 2-direction. Two inflection points are observed in the macroscopic tension stress–strain curve at axial strains of about 0.02 and 0.29 correlating to the yield of the thin (200 nm) diagonal struts and the yield of the thicker (500 nm) posts, respectively. Microscopic and local features of deformation are further illustrated in the contours of plastic strain rate shown in Figure 4b at different levels of macroscopic axial strain. Plastic flow in the microframe structure initiates in the central region of the thin diagonal struts. After initial yield, necking, neck propagation, and strain hardening in the thin struts, deformation spreads to the thick posts corresponding to the second inflection point in the macroscopic tensile curve.

Figure 5 shows the mechanical response of the microframe structure under compression. The macroscopic compression curve (Fig. 5a) exhibits a single yield point that corresponds to the yielding of the diagonal members and the internal ''buckling''

Figure 6. Simulated mechanical response of the microframe structures subjected to simple shear deformation in the 32-plane. a) Macroscopic shear stress and normal stress versus the shear strain curves. b) SEM micrograph of shear region of the microframe film and plastically deformed microfibrils [12]. c) Simulated results show contours of plastic shear strain rate at increasing levels of shear strain.

collapse of the microframe structure. Figure 5d exhibits compressed configurations of the two- and three-layer RVEs under increasing levels of macroscopic axial strain. After a critical strain, the structure collapses and the thinner struts plastically bend and rotate (also see experimental observation in Fig. 5c). The critical strains are 0.024 and 0.032 for the two- and three-layer RVEs due to the different allowable wavelength buckling

instability for each case due to the periodic boundary condition. The energy (per unit volume) absorbed during compression for these two cases are shown in Figure 5b. This result reveals the ability to also tailor and increase the energy absorption capacity of a periodic structure by forcing different buckling wavelengths (perhaps with internal structural constraints).

The mechanical response of the microframe structure during simple shear deformation is shown in Figure 6. The deformed configurations shown in Figure 6c show that the macroscopic shear strain is accommodated by plastic straining of the thin diagonal struts which then enable large scale rotation and alignment into ''rows'' of the entire structure. This deformation mechanism is suggested to account for the formation of the long fibrils observed in the experiments (see Fig. 6b).

The shear stress–shear strain behavior and corresponding normal stress–shear strain behavior are both shown in Figure 6a. As expected, at small strains, there is negligible normal stress. Once the first yield event occurs and larger strain ensues, the normal stress is found to be negative (over the range of macroscopic shear strains from 0.05 to 0.29). In contrast, for simple shear deformations of isotropic solids, the normal stress would be positive. The large negative normal stress is a result of the anisotropic microstructure and the deformation-induced changes and rotations in the microstructure. Similar negative normal stress has been observed in carbon nanotube-filled polymer nanocomposites[20] and networks of semiflexible biopolymer gels.[21] These results suggest the tailoring of microstructure to achieve prescribed normal stress evolutions during simple shear to further aid in energy absorbing mechanisms during shear deformations (where the inherent normal stress response can be used to either close up or prop open a structure during shear loading).

2.4. Beam Ratio Effects

==The topology of the microstructure clearly plays a key role in the mechanical response of microframe materials.==[22,23] ==Here, the effect of underlying geometry on the nonlinear mechanical behavior will be discussed. The beam ratio (BR) defined as the ratio of the diameter of diagonally oriented struts to the diameter of the vertical post, is a structural parameter we define to compare different microtruss and microframe materials.== The microframe structure discussed thus far has a BR = 0.4 and a volume fraction f of polymer of $f = 0.26$. For comparison purposes, five microframe structures are now simulated with BR varying from 0.4 to 1.2 while maintaining f fixed at $f = 0.26$.
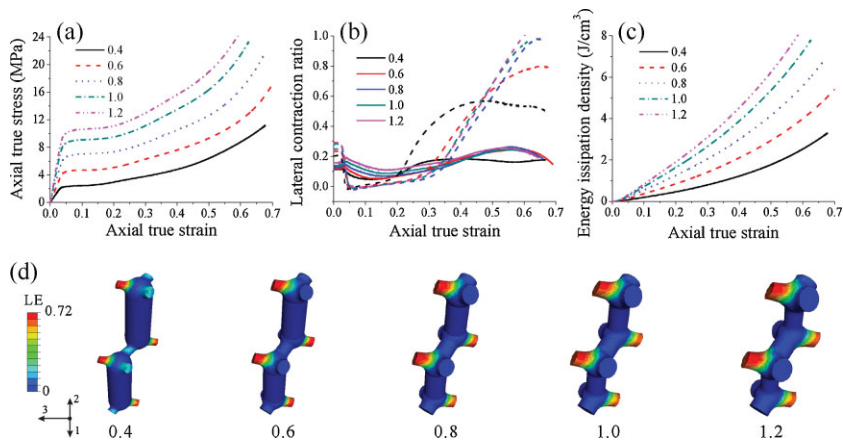
Figure 7. Micromechanical modeling results of the comparison of microframe structures with different geometries under uniaxial tension. a) Stress–strain curves in the 3-direction. b) Lateral contraction ratio relationships (1-direction: dashed lines, 2-direction: solid lines). c) Predictions of energy dissipation density as a function of microscopic tension strain. d) Contours of maximum principal true strain of the 3D RVEs with different structure ratios at a uniaxial tension strain of 0.30.

The behaviors of these structures subjected to uniaxial tension, simple shear deformation, and uniaxial compression are compared.

For the case of uniaxial tension in the 3-direction (see Fig. 7a), the Young's modulus and yield stress are found to increase with an increase in BR while the yield strain remains the same. These dependencies are direct results of the axial behavior in the 3-direction being governed by the particular diagonal member aligned with the 3-direction; the increase in diameter of this member with increase in BR gives the increase in macroscopic modulus and yield stress; the scaling of the macroscopic yield stress with modulus gives the yield strain to be relatively independent of BR. All structures show similar lateral contraction behavior as a function of axial strain (Fig. 7b). Figure 7c provides
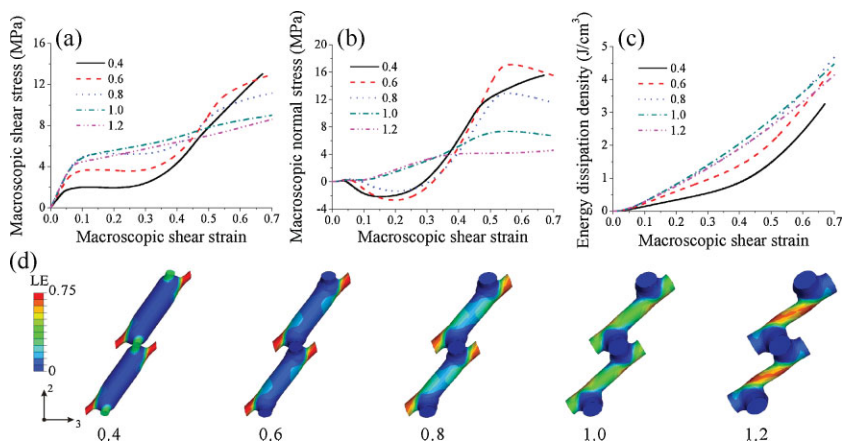
Figure 8. Micromechanical modeling results of the comparison of microframe structures with different geometries under macroscopic simple shear deformation. a,b) Shear and normal stress–strain curves under simple shear deformation in the 32-plane. c) Predictions of energy dissipation density as a function of microscopic shear strain. d) Contours of maximum principal true strain at a shear strain of 0.70.

the calculated total strain energy absorption under uniaxial tension which is shown to dramatically increase with an increase in BR at any given macroscopic strain. Contours of maximum principal true strain for the five structures at a macroscopic strain of 0.30 are shown in Figure 7d further emphasizing the dominant role of the diagonal strut aligned with the 3-direction.

For the case of simple shear, the mechanical response is dominated by the plastic stretching and rotation of various members; the members which govern this shear behavior are found to depend on BR. When BR = 0.4, 0.6, and 0.8, the thin diagonal members govern the behavior; whereas for BR larger than 1.0, yield and necking initiate in the "vertical posts" since these are now the "weaker link." Figure 8d shows the maximum principal true strain distributions for all five structures under a shear strain of 0.70 further illustrating how the deformation mechanism depends on BR. Furthermore, the normal stress behavior is seen to transition from a negative value for small BR to a positive value at the larger BR ratios (see Fig. 8b); this dependence is related to the orientation of the diagonal members and the evolution of the net section force in these members in each structure. For this type of 3D microframe structure, the mechanical balance between vertical post and diagonal member governs the linear and nonlinear behavior. Figure 8c shows the strain dependence of the calculated energy absorption. The absorption is greater in the higher BR materials compared to the 0.4 BR, but is nearly identical for the BR cases of 0.8, 1.0, and 1.2 as also seen in the nearly identical shear stress–strain curves.

For the case of uniaxial compression, the mechanical response is dominated by the structure stability and the plastic deformation of various members. When BR = 0.4, 0.6, and 0.8, a single peak strength is observed in the stress–strain curves as shown in Figure 9a, followed by a stress drop and then a long plateau, which allows energy dissipation at near constant load. These structures show the buckling-dominated behavior, arising from the plastic yielding of the diagonal members and subsequent hinge formation giving buckling, bending, and rotation (see Fig. 9c). When BR is larger than 1.0, there no longer exists a thin diagonal member and yielding initiates in the vertical posts (Fig. 9c); structural "collapse" takes a different form occurring at much greater strain where a second "peak" is seen in the computed stress–strain curve. This behavior enables the structures to absorb much more energy as shown in Figure 9b. The absorbed energy per unit volume at 25% strain is up to 4 MJ m^{-3}, which is higher than many commercially available polymer foams[4] (e.g., 3 MJ m^{-3} for a PP foam of density of 0.6 Mg m^{-3} and 1.5 MJ m^{-3} for a PU foam of density of 1.05 Mg m^{-3}), whereas the density of the microframe structure in this study is only 0.3 Mg m^{-3}. Hence, the corresponding energy absorption per unit mass at 25% strain is 13.3 MJ Mg^{-1} for our microframe compared to 5.0 and 1.4 MJ Mg^{-1} for the commercially available PP and PU foams.

In most applications, the selection and design of cellular solids for energy absorption depend on the specification of the problem. Here it is shown that, at a given density, the modulus, yield stress, and energy absorption can be further optimized by tailoring the geometry of microframe structures which can be controlled by interference lithography to meet different requirements (see Appendix for the comparison of the relative modulus and the collapse stress of a cellular solid from our simulations and existing theoretical models for idealized geometries).

3. Conclusions

In summary, fully three-dimensional micromechanical models of microframe structures have enabled the quantitative investigation of the macroscopic response and underlying plastic dissipation mechanisms in microframe-structured polymers subject to very large strain deformation histories. The simulations successfully predict the deformation mechanisms observed experimentally and provide the corresponding macroscopic stress–strain behaviors for arbitrary load histories, quantifying elastic, yield, and post-yield dissipation behavior. The results highlight important features of the inelastic behaviors of these structures including i) the ability to utilize the strain hardening plasticity of the polymer to spread deformation throughout the structure enabling dissipative pathways prior to localized failure; ii) the ability to utilize the microstructure to tailor the lateral contraction behavior, not just at small strains, but also during large inelastic deformations; iii) the ability to tailor the microstructure to achieve either positive or negative normal stress behavior during simple shear; iv) the ability to optimally structure the material (e.g., at fixed density) to achieve desired nonlinear anisotropic mechanical performance as well as maximum energy absorption.
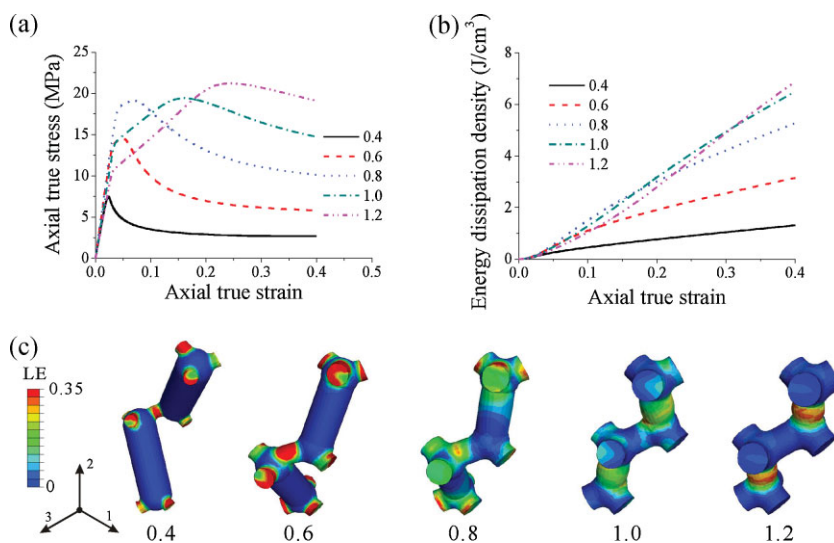
Figure 9. Micromechanical modeling results of the comparison of microframe structures with different geometries under macroscopic compression. a) Stress–strain curves under uniaxial compression in the 2-direction. b) Predictions of energy dissipation density as a function of microscopic compression strain. c) Contours of maximum principal true strain at a compression strain of −0.20.

FULL PAPER
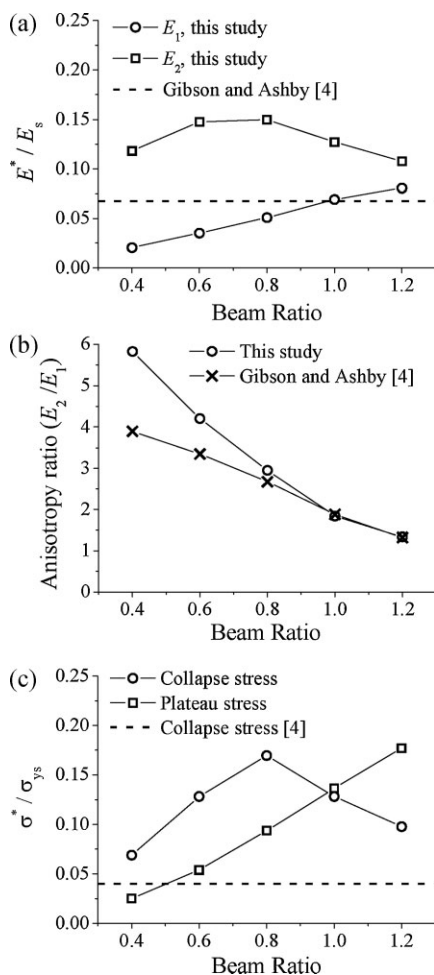
Figure 10. Comparison of the results of a cellular solid of relative density $\rho^*/\rho_s = 0.26$ as calculated for the different BR materials of this paper and as calculated from idealized open-cell cubic model [4]. a) The relative modulus normalized by the solid modulus (equiaxed cubic cell for Gibson–Ashby data). b) The modulus anisotropy ratio (elongated cubic cell for Gibson–Ashby data). c) The initial plastic collapse stress and plateau stress normalized by the yield strength of the solid (equiaxed cubic cell for Gibson–Ashby data).

tors.[4,23–25] The Gibson–Ashby model[4] assumes a cubic RVE of beams and finds $n = 2$ and C to be close to 1 if the struts are fully dense.

For the polymer microframes reported in this paper, the relative density is fixed to be 0.26. The simulated Young's modulus varies from 67 to 266 MPa in the 1-direction and 355–495 MPa in the 2-direction, which depends on BRs. Figure 10 shows the comparison of the relative modulus and the plastic collapse stress from our simulation and the idealized cubic open-cell cellular model.[4]

Acknowledgements

[1] P. J. Hogg, *Science* **2006**, *314*, 1100.

[2] A. B. Dalton, S. Collins, E. Munoz, J. M. Razal, V. H. Ebron, J. P. Ferraris, J. N. Coleman, B. G. Kim, R. H. Baughman, *Nature* **2003**, *423*, 307.

[3] A. Y. Cao, P. L. Dickrell, W. G. Sawyer, M. N. Ghasemi-Nejhad, P. M. Ajayan, *Science* **2005**, *310*, 1307.

[4] L. J. Gibson, M. F. Ashby, *Cellular Solids: Structure and Properties*, 2nd ed., Cambridge University Press, Cambridge **1999**.

[5] J. Aizenberg, J. C. Weaver, M. S. Thanawala, V. C. Sundar, D. E. Morse, P. Fratzl, *Science* **2005**, *309*, 275.

[6] Y.-H. Ha, R. A. Vaia, W. F. Lynn, J. P. Costantino, J. Shin, A. B. Smith, P. T. Matsudaira, E. L. Thomas, *Adv. Mater.* **2004**, *16*, 1091.

[7] M. C. M. Van der Sanden, H. E. H. Meijer, P. J. Lemstra, *Polymer* **1993**, *34*, 2148.

[8] C. Y. Wen, W. S. Kim, E. L. Thomas, unpublished.

[9] E. J. Kramer, L. L. Berger, *Adv. Polym. Sci.* **1990**, *91–92*, 1.

[10] M. C. M. Van der Sanden, H. E. H. Meijer, *Polymer* **1993**, *34*, 5063.

[11] T. Choi, J.-H. Jang, C. K. Ullal, M. C. LeMieux, V. V. Tsukruk, E. L. Thomas, *Adv. Funct. Mater.* **2006**, *16*, 1324.

[12] J.-H. Jang, C. K. Ullal, T. Choi, M. C. LeMieux, V. V. Tsukruk, E. L. Thomas, *Adv. Mater.* **2006**, *18*, 2123.

[13] M. Danielsson, D. M. Parks, M. C. Boyce, *J. Mech. Phys. Solids* **2002**, *50*, 351.

[14] M. Danielsson, D. M. Parks, M. C. Boyce, *J. Mech. Phys. Solids* **2007**, *55*, 533.

[15] M. C. Boyce, D. M. Parks, A. S. Argon, *Mech. Mater.* **1988**, *7*, 15.

[16] E. M. Arruda, M. C. Boyce, *Int. J. Plasticity* **1993**, *9*, 697.

[17] E. M. Arruda, M. C. Boyce, *J. Mech. Phys. Solids* **1993**, *41*, 389.

[18] R. Feng, R. J. Farris, *J. Micromech. Microeng.* **2003**, *13*, 80.

[19] J. B. Choi, R. S. Lakes, *J. Mater. Sci.* **1992**, *27*, 4678.

[20] S. B. Kharchenko, J. F. Douglas, J. Obrzut, E. A. Grulke, K. B. Migler, *Nat. Mater.* **2004**, *3*, 564.

[21] P. A. Janmey, M. E. Mccormick, S. Rammensee, J. L. Leight, P. C. Georges, F. C. Mackintosh, *Nat. Mater.* **2007**, *6*, 48.

[22] A. G. Evans, J. W. Hutchinson, N. A. Fleck, M. F. Ashby, H. N. Wadley, *Prog. Mater. Sci.* **2001**, *46*, 309.

[23] M. Maldovan, C. K. Ullal, J.-H. Jang, E. L. Thomas, *Adv. Mater.* **2007**, *19*, 3809.

[24] R. M. Christensen, *J. Mech. Phys. Solids* **1986**, *34*, 563.

[25] W. E. Warren, A. M. Kraynik, *J. Appl. Mech.* **1988**, *55*, 341.

Appendix

The Young's modulus, E^*, of open-cell cellular solid (with random and isotropic cellular microstructure) have been found to be related to their density, ρ^*, relative to the solid density, ρ_s, and the Young's modulus of the solid, E_s, via

$$\frac{E^*}{E_s} = C\left(\frac{\rho^*}{\rho_s}\right)^n \tag{1}$$

where C and n can be obtained by fits to experimental data. Models based on idealized microstructures have been proposed by several investiga-

© 2009 WILEY-VCH Verlag GmbH & Co. KGaA, Weinheim